ELSEVIER

Journal of Structural Geology 28 (2006) 695–712

JOURNAL OF STRUCTURAL GEOLOGY

www.elsevier.com/locate/jsg

3-D deformation pattern analysis and evolution of the Añisclo anticline, southern Pyrenees

S. Tavani [a,*], F. Storti [a], O. Fernández [b], J.A. Muñoz [b], F. Salvini [a]

[a] *Univeristà degli studi "Roma Tre", Dipartimento di Scienze Geologiche, Largo S.L. Murialdo 1, 00146 Rome, Italy*
[b] *Grup de Geodinàmica i Anàlisi de Conques, Departament de Geodinàmica i Geofísica, Universitat de Barcelona, 08028 Barcelona, Spain*

Received 7 February 2005; received in revised form 5 October 2005; accepted 28 January 2006
Available online 13 March 2006

Abstract

Understanding the genetic relationships of folding-related deformation structures is of importance for both academic and industrial purposes. We analysed the three-dimensional deformation pattern of the Añisclo anticline, in the southern Pyrenees. The specifically designed statistical method includes sequential steps of statistical and spatial data analysis and classification. Our results indicate that pressure solution cleavage frequency exhibits a spatial distribution that depends on the position within the fold. Conversely, such a dependence does not occur in joints and veins. Consequently, our data suggest that pressure-solution cleavage is the most appropriate deformation structure for unravelling fault-fold kinematics in carbonate multilayer. In particular, we found that the spacing of solution cleavages (S) is related to the corresponding bed thickness (H). This supports the use of H/S value for deformation intensity quantification instead of spacing. In the Añisclo anticline, analysis of H/S indicates the occurrence of three main deformation panels whose restoration suggests that fold evolution progressed from layer-parallel shortening, to décollement folding, up to thrust breakthrough, and fault-propagation folding. Comparison of H/S values with finite strain data indicates that line-length was not preserved during fold evolution. This evidence has important implications for the kinematic interpretation of layer-parallel shortening and cross-section balancing.

Keywords: Thrust-related folding; Brittle deformation analysis; Layer-parallel shortening; Cross-section balancing; Pyrenees

1. Introduction

Development of structures in thrust-related folds is controlled by several factors including the environmental conditions of deformation (e.g. Chester et al., 1991; Stewart and Alvarez, 1991; Jamison, 1992; Lemiszki et al., 1994; Woodward, 1999), the mechanical stratigraphy of the folded multilayer (e.g. Corbett et al., 1987; Woodward and Rutherford, 1989; Protzman and Mitra, 1990; Gross, 1995; Couzens and Wiltschko, 1996; Fischer and Jackson, 1999; Chester, 2003), and the folding mechanism (e.g. De Sitter, 1956; Ramsay, 1974; Sanderson, 1982; Dahlstrom, 1990; Srivastava and Engelder, 1990; Fischer et al., 1992; Apotria et al., 1996; Storti and Salvini, 1996; Salvini and Storti, 2001). Comprehensive understanding of the relationships between the folding process and the development in time and space of folding-related structures is of importance for both academic and industrial purposes. Understanding these relationships sets reliably constraints on fault-related fold kinematics and favours the development of unique section-balancing solutions (e.g. Thorbjornsen and Dunne, 1997; Salvini and Storti, 2004). Similarly, these relationships impact our understanding on the migration and accumulation of fluid with respect to fold formation and, consequently, the development of hydrocarbon and water reservoirs. These relationships have been investigated by using the spatial distribution of microstructural features (e.g. Allmendinger, 1982; Couzens and Dunne, 1994; Fisher and Anastasio, 1994; Hedlund et al., 1994; Anastasio et al., 1997), finite strain data (e.g. Fisher and Coward, 1982; Mitchell and Woodward, 1988; Protzman and Mitra, 1990; Couzens and Dunne, 1994; Thorbjornsen and Dunne, 1997; Mukul and Mitra, 1998; Yonkee, 2005), and the characterisation of mesostructural patterns in different fold sectors (e.g. Srivastava and Engelder, 1990; Cooper, 1992; Fischer et al., 1992; Erslev and Mayborn, 1997; Jamison, 1997; Tavernelli, 1997; Thorbjornsen and Dunne, 1997; Storti and Salvini, 2001).

In this work, we show that systematic statistical analysis of folding-related structures, both across and along the fold trend, provides the necessary information to constrain fault-fold kinematic history. We propose a working method focused on

* Corresponding author. Tel.: +39 654888049; fax: +39 654888201.
E-mail address: tavani@uniroma3.it (S. Tavani).

0191-8141/$ - see front matter © 2006 Elsevier Ltd. All rights reserved.
doi:10.1016/j.jsg.2006.01.009

the quantitative analysis of mesoscopic structures. The approach combines spatial statistics of data from structural transects (i.e. Salvini et al., 1999) with cumulative data analysis in frequency histograms and equal-area Schmidt stereonets. The approach is applied to the Añisclo anticline, in the southern Pyrenees, to unravel its kinematic history, which includes layer surface variations (i.e. line-length variations in cross-section) through time. Implications for the non-preservation of line-length in section balancing of thrust-related folds are considered.

2. Methodology

Structural data are collected in closely spaced georeferenced field sites (data location was accomplished with GPS equipment), where structures are characterised by their orientation, overprinting relationships, spacing (the distance between adjacent surfaces, *S*), termination or non-termination at bedding, and geometric relationships to bedding as defined by angle to bedding (ATB). Veins are also characterised by their aperture (*A*) (Fig. 1a). Data about stratabound structures

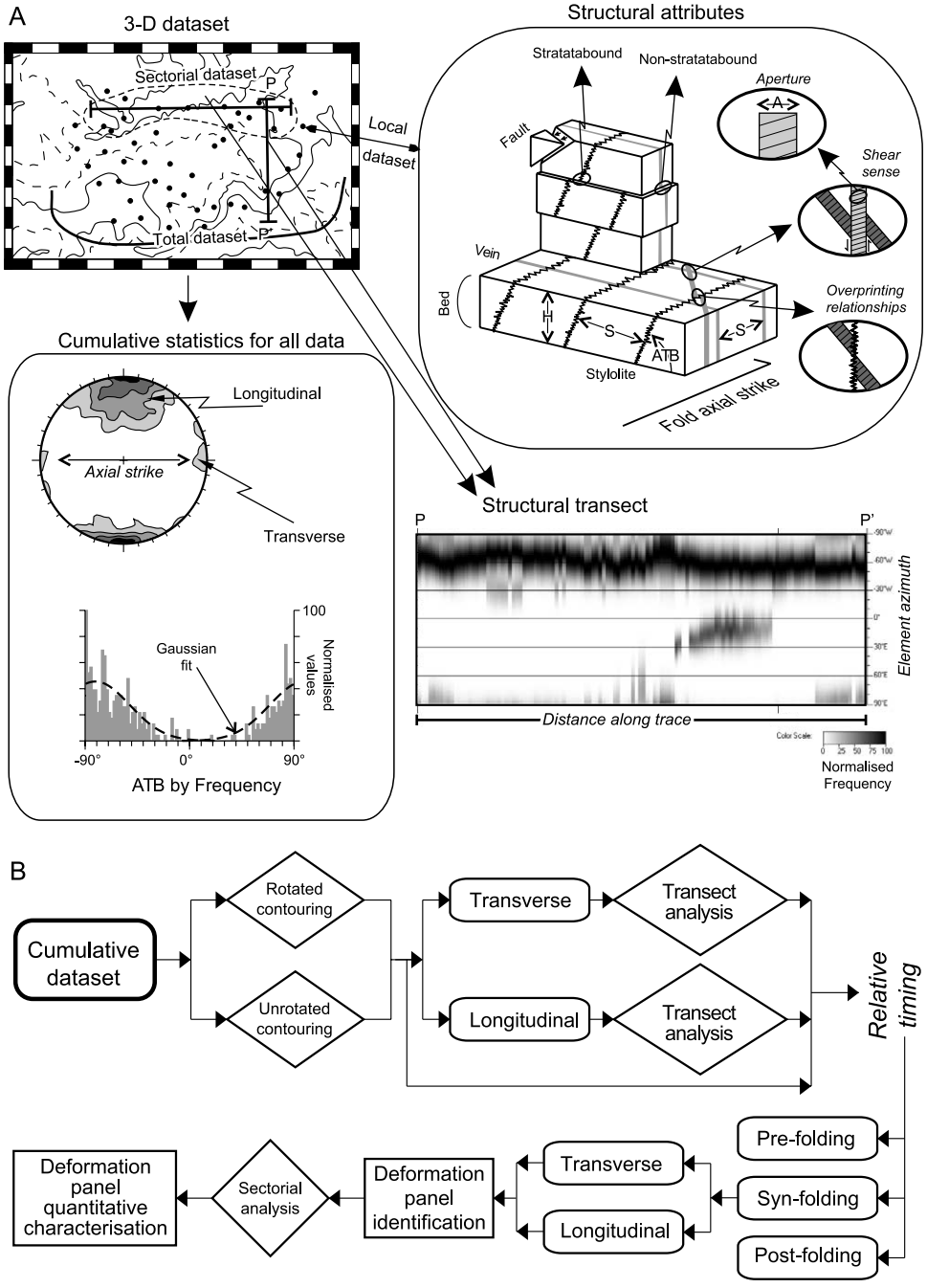

Fig. 1. Proposed working strategy for statistical data analysis. (A) Structural attributes and related analytical tools. (B) Flow diagram illustrating the sequential steps for data analysis and interpretation. *H* = bed thickness; ATB = angle to bedding; *S* = spacing; *A* = aperture. See text for details.

include thickness of boundary layer (*H*; Fig. 1a) to normalise their spacing by computing the *H*/*S* ratio, which is numerically equivalent to the *C*/*B* fissility of Durney and Kisch (1994). In particular, our dataset shows that the spacing of pressure-solution cleavage in the Añisclo anticline relates to the corresponding bed thickness (Fig. 2). This supports the use of the normalised spacing of solution cleavage (*H*/*S* ratio) to compare deformation intensities between different fold sectors.

The first step of the proposed methodology (Fig. 1) is to merge the entire dataset into a database from which the orientation of a type of structure with respect to the fold axial trend is investigated by data contouring on equal-area Schmidt stereonet (Fig. 1). To account for the presence of steeply dipping beds, data are rotated by restoring the reference bedding surfaces to the horizontal (Ramsay, 1967).

Cumulative data contouring allows the identification of longitudinal and transverse structures and their classification into separate sets. The spatial variability of both angle to bedding and frequency is investigated, for each set, by using structural transects (Salvini et al., 1999; Tavani et al., 2004). Data from an area of interest are projected onto the transect, orthogonally to the transect direction. The transect length is divided into *N* cells of a given width, and for each cell a frequency histogram of the analysed parameter is produced. For a graph of transect results, the *X*-axis represents the position along the transect trace, the *Y*-axis represents the parameter value, and a grey-tones scale represents the frequency associated with each *Y* value, normalised to 100 (e.g. Fig. 1a for bedding azimuth). The along-transect smoothing of the resulting scatterograms significantly improves their interpretation. Eventually, a uni/polimodal Gaussian best fit is applied to each cell histogram.

The determination of the relative ages of structures to the hosting fold from crosscutting field relationships is improved by comparison of cumulative statistical and transect analyses (Fig. 1b). Statistically, structures are identified as syn-folding when the spatial variability of their characteristics is a function of change in fold geometry. This functionality is identified by the correlation of variability to domains (i.e. deformation panels) of the fold (Storti and Salvini, 1996; Salvini and Storti, 2001). Average structure orientation is determined from stereoplots and average and standard deviation of characteristics, such as ATB, *H*/*S* and *S* are determined from histograms. We use sequential restoration of deformation panels and fold geometry to unravel the progressive evolution of the host thrust–fold pair (Salvini and Storti, 2004).

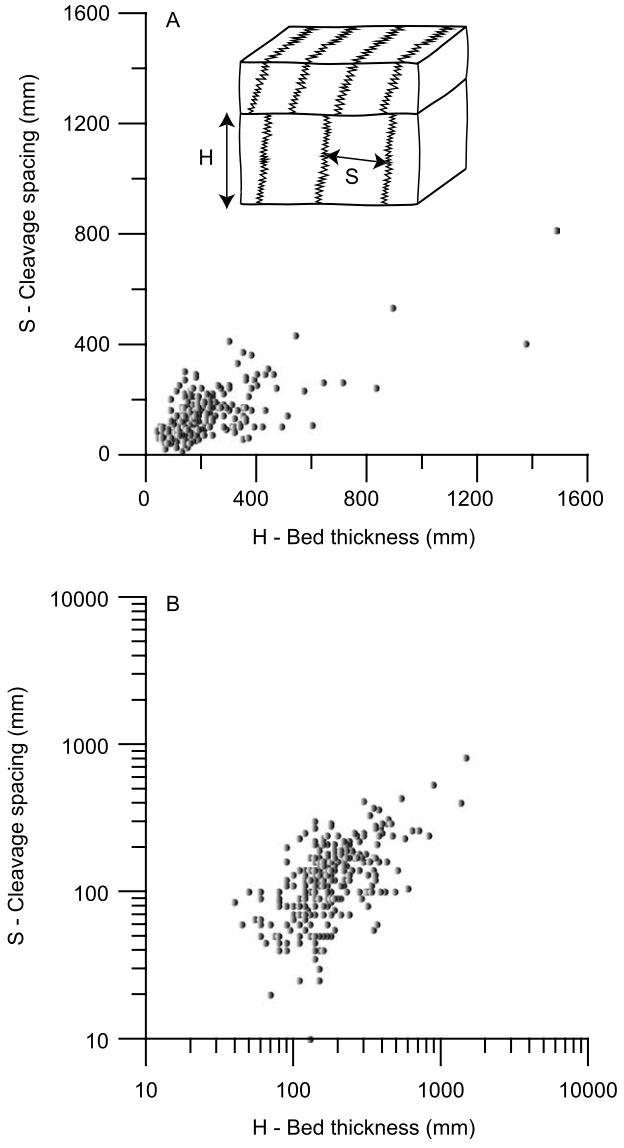

Fig. 2. Cleavage spacing versus bed thickness scatterograms in the normal (a) and bi-logarithmic space (b).

3. Geological setting of the Añisclo anticline

The N–S-trending (N 171°), Middle Eocene Añisclo anticline is located in the Spanish Pyrenees (Fig. 3a) and is part of an oblique to transverse set of fold and thrust structures along the eastern margin of the Gavarnie thrust sheet in the footwall of the Montsec thrust sheet (Fig. 3). This thrust sheet is a major feature of the western central Pyrenees (Seguret, 1970) and involves Hercynian basement rocks north of the Añisclo anticline. Its floor thrust climbs up-section southward from basement into Triassic evaporites and shales and emerges in the Sierras Exteriores at the Pyrenean thrust front (Millán, 1996; Teixell, 1996). Paleomagnetic data reveal that the Añisclo anticline and neighbouring oblique anticlines have rotated up to 80° in a clockwise direction during and after their growth (Dinarès Turell, 1992; Parés and Dinarès Turell, 1993; Pueyo et al., 2004). This indicates that these structures originally formed with roughly E–W trend as frontal structures and then were rotated to their current orientation (Fernandez, 2004). The multilayer involved in the Añisclo anticline includes alternating limestones and marls of Upper Cretaceous to Middle Eocene age overlying the Keuper Triassic evaporites (e.g. Garrido and Rios, 1972; Rios et al., 1982) (Fig. 3b). The Lutetian San Vicente turbidites lie mostly unconformably over this sequence and are partially coeval with the growth of the Añisclo anticline (e.g. Fernández et al., 2004).

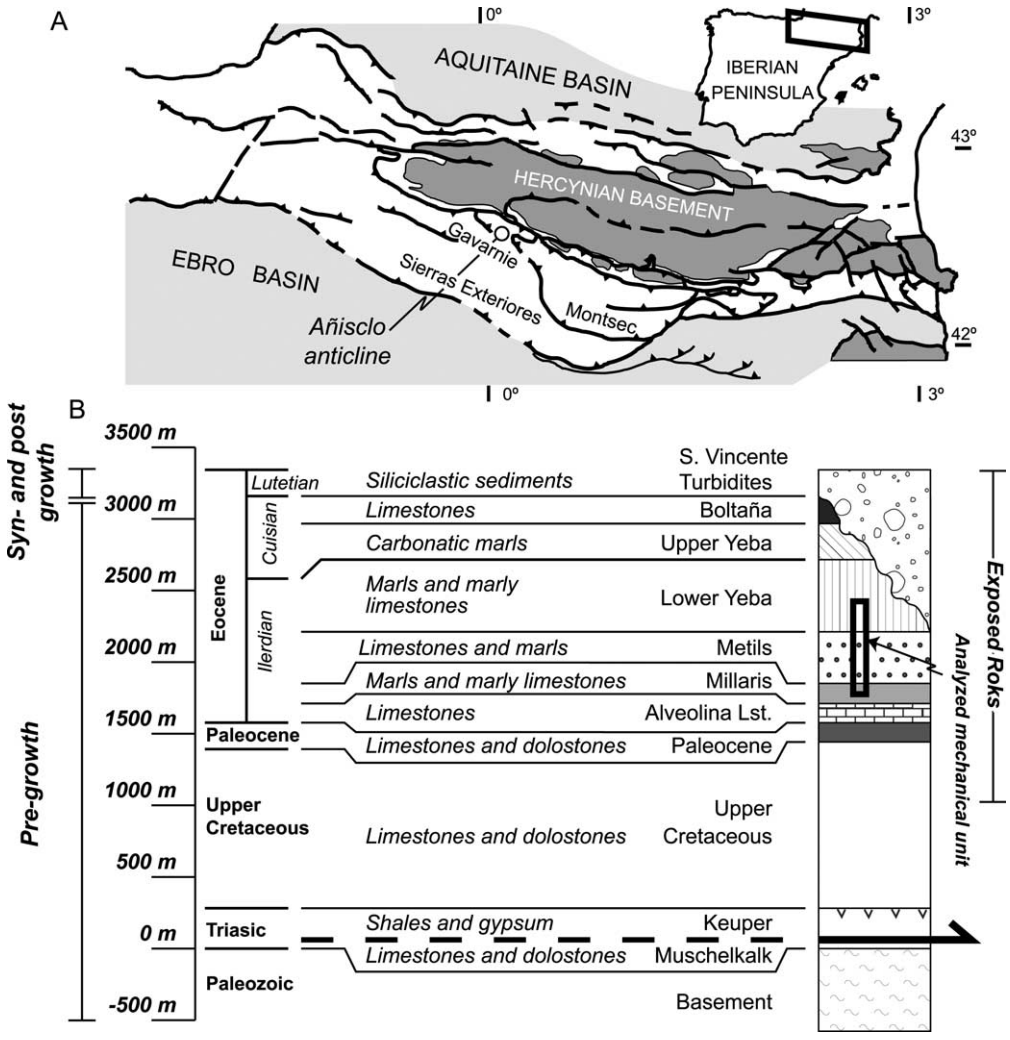

Fig. 3. (a) Schematic geological map of the Pyrenees with location of the study area. Gavarnie, Sierras Exteriores and Montsec are the major foreland thrust sheets in the central Spanish Pyrenees. (b) Stratigraphic succession in the Añisclo anticline area.

In the northern sector, the geometry of the Añisclo anticline is nearly symmetrical and developed by décollement folding (Fig. 4) (Holl and Anastasio, 1995). Our study area includes the central and southern sectors of the Añisclo anticline, where the fold geometry is more complex. The anticline plunges southward at about 10° until increasing to 25° in its southernmost termination. The backlimb of the Añisclo anticline is characterised by bedding dip ranging from 20 to 45° toward the east and by a gentle transition to a nearly flat-lying crest (Fig. 5). The crest–forelimb transition in the oldest exposed rocks is commonly coincident with an intensely deformed zone, which is interpreted to be associated with a steep splay of the main Añisclo thrust. The forelimb in the northern sector of the anticline has a nearly constant southwestward dip of about 30°. The central sector is characterised by a curvilinear shape that progressively reaches an overturned attitude of 65° to the east and then curves to a moderate westward dip before transitioning westward to the flat-lying foreland. Late-stage extension faults strike oblique to the fold axis across both the backlimb and forelimb. Accordingly, they may cut through the Añisclo thrust down to the basal thrust of the Gavarnie thrust sheet (Fig. 5). However, these extension faults may reactivate part of the Añisclo thrust below the forelimb. To the south, the anticline terminates with a vertical-axis cone geometry, dips ranging from 45° to the southwest in the forelimb to 25° to the southeast in the backlimb.

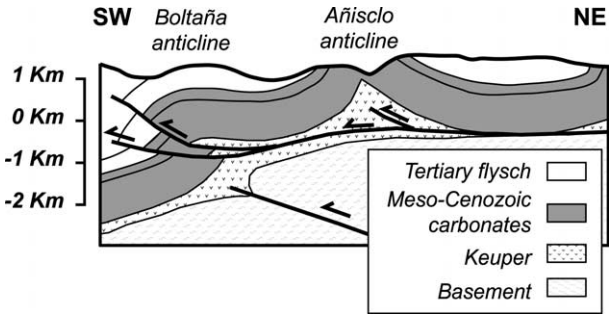

Fig. 4. Balanced cross-section across the northern sector of the Añisclo anticline (from Holl and Anastasio, 1995).

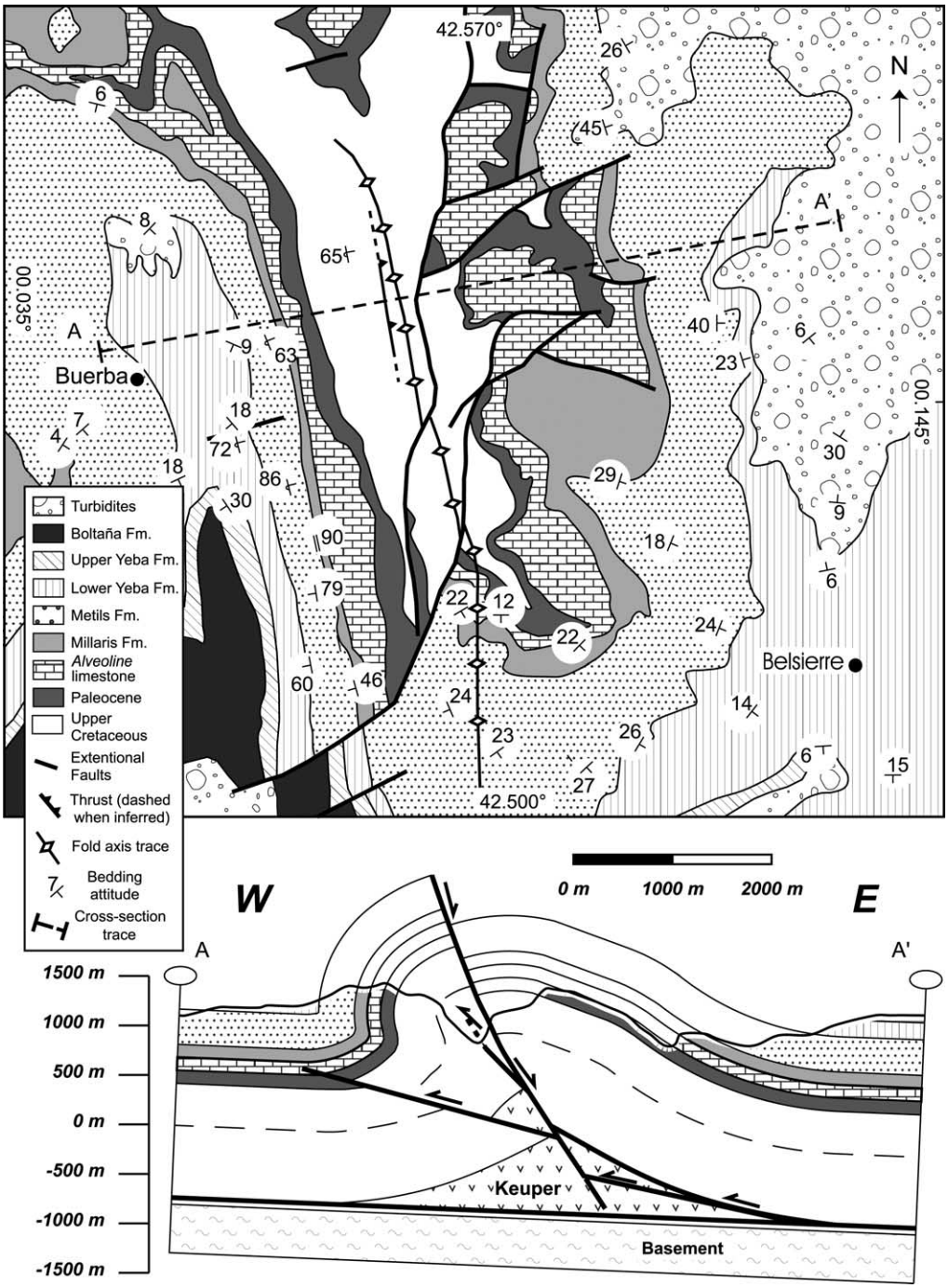

Fig. 5. (a) Geological map of the Añisclo anticline area (after Rios et al., 1982). (b) Balanced cross-section across the central sector of the Añisclo anticline.

4. Structural data

Sixty-six georeferenced field sites were located in four structural domains (Fig. 6). In all the cases, marly limestones were sampled to minimise effects of lithologic variations (e.g. Fischer and Jackson, 1999) from the lower Eocene portion of the stratigraphic sequence that was deposited before folding (Figs. 3b and 5). Bed thicknesses range from 5 to 50 cm and average 15 cm. The analysed structures include pressure-solution cleavages, joints, veins and faults. In the following, their strike is represented as a clockwise angle from the north (0–180°).

Solution cleavages are stratabound undulatory surfaces enhanced in exposure by weathering. Their spacing is nearly constant at the outcrop scale (Fig. 7). Conversely, joints, veins and faults are both stratabound and non-stratabound and their spacing varies. Transverse hairline veins occur with cleavage surfaces, their spacing varies strongly and generally their dimensions are less than bed thickness and cleavage spacing. The variability of hair-line veins geometry and timing cannot be easily related to fold kinematics and were not analysed. Instead, non-stratabound veins were analysed. Field observations of mutually crosscutting relationships between the

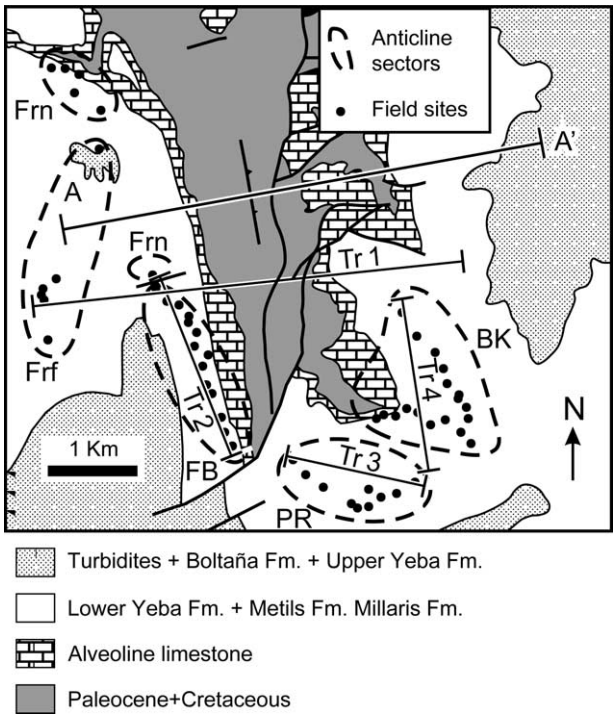

Fig. 6. Field site distribution within the five main sectors recognised in the study area. Tr: transect trace. Frf: far foreland; Frn: near foreland; PR; southern periclinal termination; BK: backlimb.

main solution cleavage set and joints/veins and faults (Fig. 8) support the interpretation that they developed coevally.

Cumulative contouring on an equal-area stereonet of poles to joint/vein, faults and pressure-solution cleavage highlights the presence of two azimuthal sets (Fig. 9a). The former includes pressure solution cleavages striking about parallel to the fold axial trend (Type 2 fractures; Stearns, 1968), whilst the latter includes joints/veins and faults striking at high angle to the fold axial trend (Type 1 fractures; Stearns, 1968). Both the sets exhibit lower data scattering in the rotated analysis with respect to the unrotated one. In particular, rotated azimuth and dip frequency distributions of both cleavage and joint/vein and fault are characterised by a standard deviation comparable with or lower than the corresponding unrotated analysis (Fig. 9b). In the rotated analyses, the standard deviations of cleavage azimuth and dip are quite high and comparable, i.e. there is an intrinsic variability in cleavage orientation related to its undulated geometry. Conversely, the standard deviation of joint/vein and fault dip is much lower than the corresponding azimuth standard deviation. This difference likely relates to the typical occurrence of three subsets within Type 1 fractures, i.e. tensile structures bisecting a conjugate strike slip fault set (e.g. Stearns, 1968; Hancock, 1985; Cooper, 1992). Accordingly, we fitted the joint, vein and fault azimuth frequency distribution with three Gaussian curves. The obtained azimuthal values of 82° (±10°), 55° (±15°) and 116° (±10°) support the occurrence of the three subsets within Type 1 fractures (Fig. 9c). In particular, the NE–SW oriented fault sets is interpreted to have a right-lateral strike-slip kinematics and the ESE–WNW fault set is interpreted to have a left-lateral strike-slip kinematics. These fault sets are bisected by E–W tensile structures. This interpretation is supported by the occurrence in the field of faults at the mesoscale, showing comparable distribution of orientation and kinematics (Figs. 8a and 9c). The standard deviations of the three azimuthal subsets are comparable with that obtained for the dip value analysis

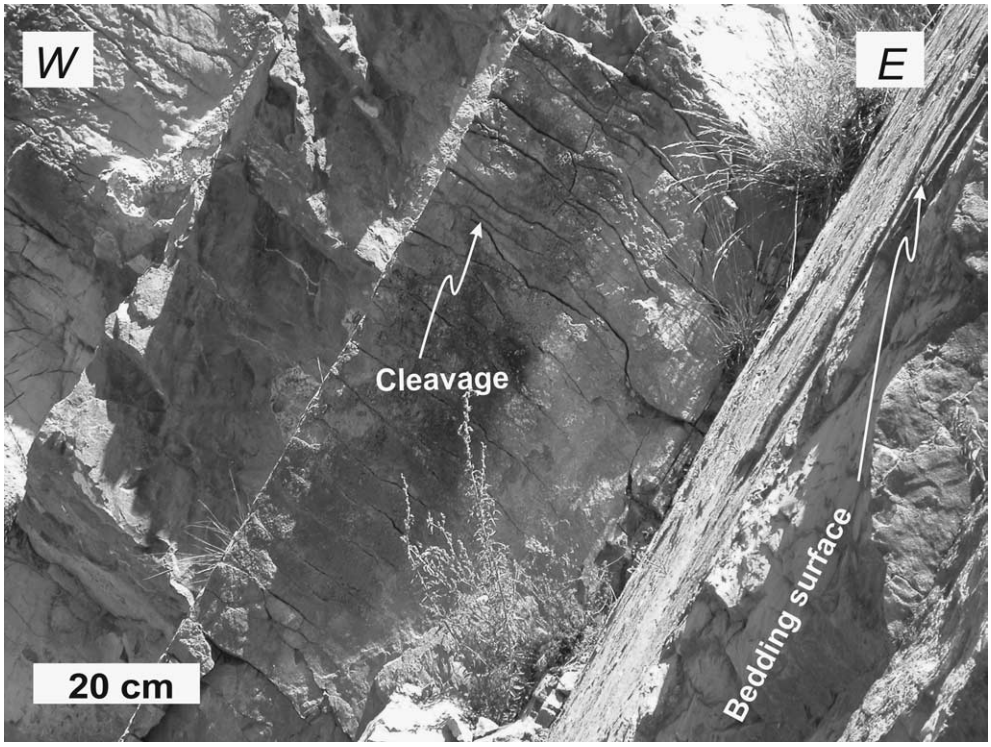

Fig. 7. Examples of spaced solution-cleavage surfaces in the forelimb of the Añisclo anticline, Metils Fm.

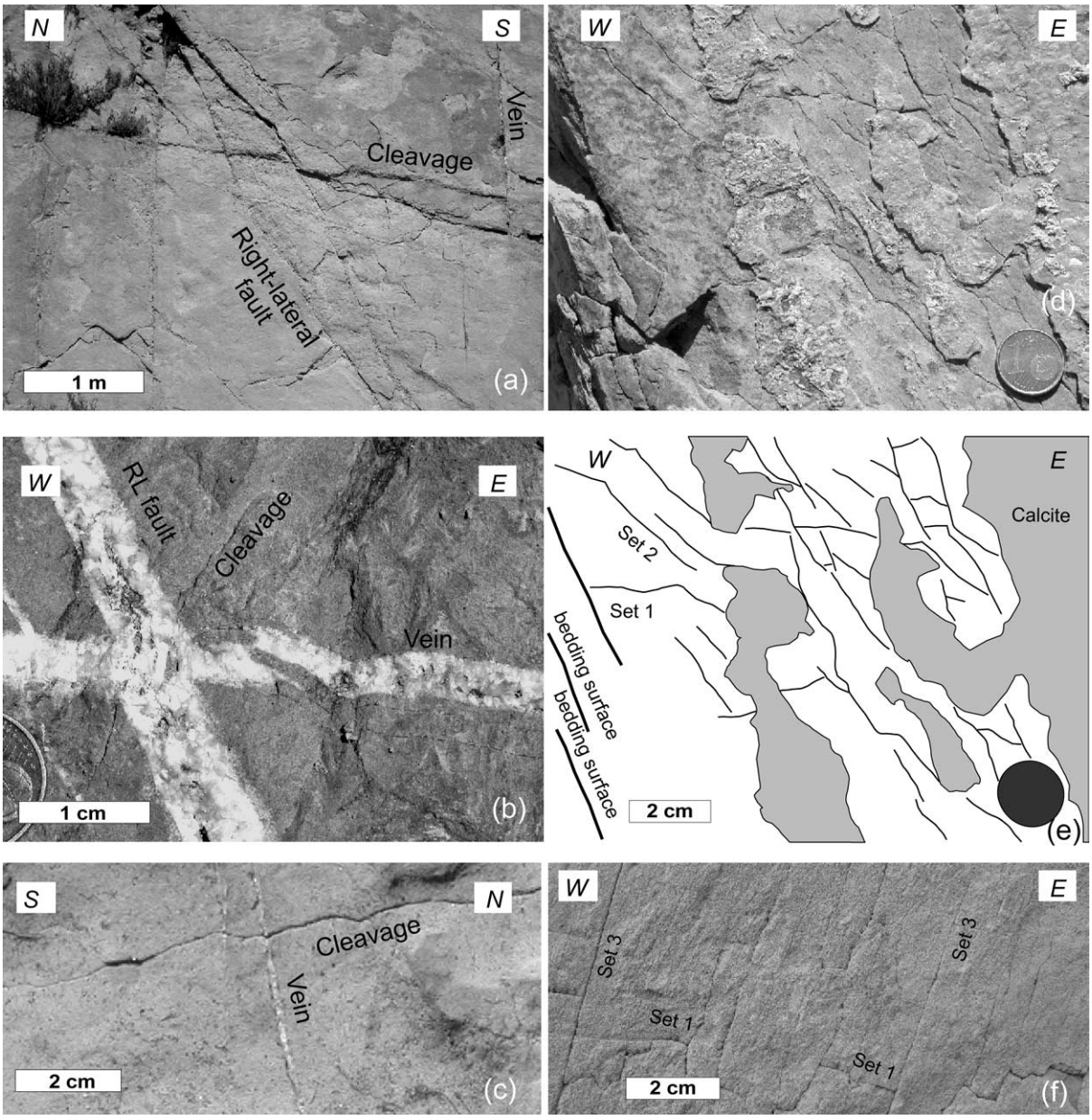

Fig. 8. Example of structural crosscutting relationships. (a) Right-lateral faults offsetting longitudinal solution cleavage on a nearly vertical bedding surface. (b) Transverse vein offsets a right lateral strike-slip fault that offsets a longitudinal solution cleavage surface. (c) Longitudinal pressure solution cleavage surface crosscutting a transverse vein. Picture (d) and line-drawing (e) of bedding-parallel pressure solution cleavage (set 3) overprinting cleavage oblique to bedding (set 2) overprinting in turn cleavage perpendicular to bedding (set 1) in the overturned forelimb. (f) Bedding-parallel pressure solution cleavage (set 3) overprinting cleavage perpendicular to bedding (set 1) in the nearly vertical forelimb.

and are significantly lower than the corresponding one for cleavage.

The across-strike transect analysis of the dataset (Fig. 1b) shows that the ATB of joint/vein and fault has nearly constant averages close to 90° all around the anticline (Fig. 10). Angle to bedding shows a greater variability for solution-cleavage surfaces. The distribution of joint/vein and fault spacing across the fold is characterised by data scattering and by the lack of clear relationships to structural position (Fig. 10). The aperture of longitudinal veins is rather constantly distributed and is about 5 mm. On the other hand, the distribution of cleavage *H*/*S* differs between fold sectors (Fig. 10).

4.1. Deformation panels

Analysis of the spatial variability of structure attributes allows the recognition of deformation panels across the anticlinal strike (e.g. Salvini and Storti, 2004). Data in Fig. 10 show that solution has a spatial variability related to the structural position within the anticline. The backlimb, the crest in the southern periclinal closure and the far foreland (sites at a distance greater than 500 m from the forelimb–foreland transition) exhibit a unimodal distribution of *H*/*S* with an average value of about 1, whereas the forelimb and the near foreland are characterised by the increase of both the *H*/*S*

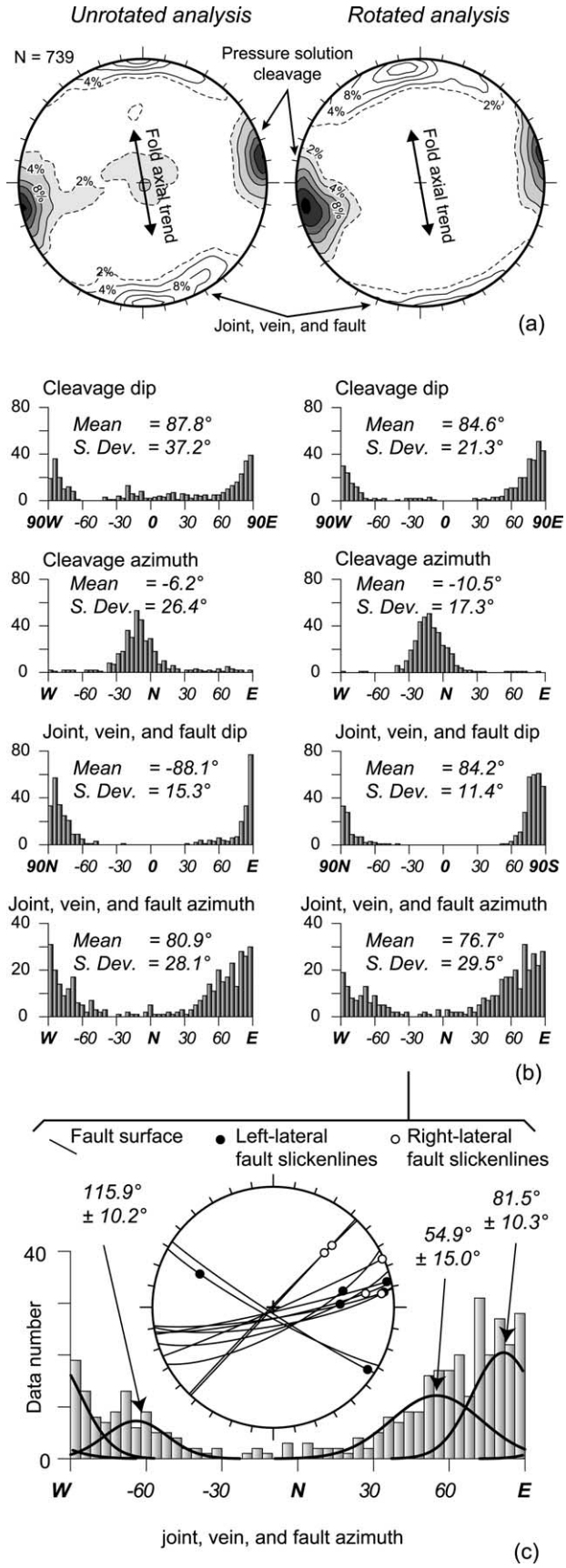

Fig. 9. Cumulative data analysis. (a) Contouring of total poles to solution cleavages, joints/veins and faults, with reference frame of unrotated and rotated bedding. (b) Frequency analysis of structures azimuth and dip. (c) Gaussian best fit of joint, vein and fault azimuth, and stereoplot of mesoscopic strike-slip faults showing the occurrence of NE–SW right-lateral strike-slip faults and NW–SE left-lateral strike-slip faults. ENE–WSW faults are more abundant and show both right-lateral and left-lateral sense of shear. They are interpreted as tear faults.

average value and data scattering. Cleavage ATB shows a distinctive behaviour in the near foreland. Furthermore, the forelimb is characterised by the peculiar occurrence of right-lateral strike-slip faults and by the absence of left-lateral strike-slip ones. All these observations concur to identify three major deformation panels across the Añisclo anticline: the near foreland (1), the forelimb (2) and the crest/backlimb (3) (Fig. 10).

In the near foreland panel, a set of solution cleavage strikes 169° (±12°) and is nearly normal to bedding (ATB of 81±12°) (Fig. 11). If a linear through the origin fit is adopted for the *H*, *S* dataset of this solution cleavage set, the regression line slope is 0.72, with a RMS of 2045. The 0 slope regression line (i.e. *S* is assumed to be independent of *H*) has a *Y*-intercept of 131 (RMS is 2370). A second solution cleavage set strikes 174° (±10°) and has an average ATB of 53° (±14°); it has a regression line slope of 0.3, with a RMS of 1598. For a linear through the origin fit the regression lines have a *Y*-intercept of 93 (RMS is 1370). The cleavage *H*/*S* data are not unimodal and their average value is about 2.1 (±1.2), being 1.7 (±0.8) and 3.3 (±1.5) for the *H*/*S* values associated with the normal to bedding and oblique sets, respectively. Crosscutting relationships indicate that the eastward-dipping cleavage is the younger one, as it consumpts the normal to bedding cleavage. Joints/veins and faults have maxima striking orthogonal (87±8°), oblique (124±10°) and parallel (177±7°) to the fold axis (Fig. 11). They correspond to transverse joints/veins, left-lateral faults and longitudinal joints/veins, respectively. The first two sets are mainly orthogonal to bedding (ATB is 88±10° and 85±7°, respectively), while the latter comprises both nearly vertical (92±11°) and westward dipping (56±5°) surfaces. The average spacing is 1026 mm (±521 mm) for transverse joints/veins, 845 mm (±357 mm) for left-lateral faults and 895 mm (±543 mm) for longitudinal joints/veins.

In the forelimb, solution cleavage has three sets (Fig. 8d and e): the first strikes 172° (±27°) and is perpendicular to bedding (ATB is 89±7°). The second, younger set, strikes 179° (±18°) and is oblique to bedding (ATB is 152±9°) (Fig. 11). The third set is bedding parallel and overprints the other two sets. In the forelimb, a large standard deviation value characterises the azimuthal distribution of the first cleavage set because, in many sectors, the dip is around 0, thus implying a large local variability of the azimuth datum. The *H*, *S* dataset of this cleavage set has a regression line with a slope of 0.48 (RMS is 3687); the horizontal regression line has a *Y*-intercept of 111 (RMS is 4372). The distribution of the *H*/*S* ratio is not unimodal with an average value of 2.3 (±1.2). These *H*/*S* data are characterised by a large variability along the forelimb (Fig. 12, transect 2). The second and the third cleavage sets are numerically much less than the first one and mainly developed in clay-rich layers where data were not collected.

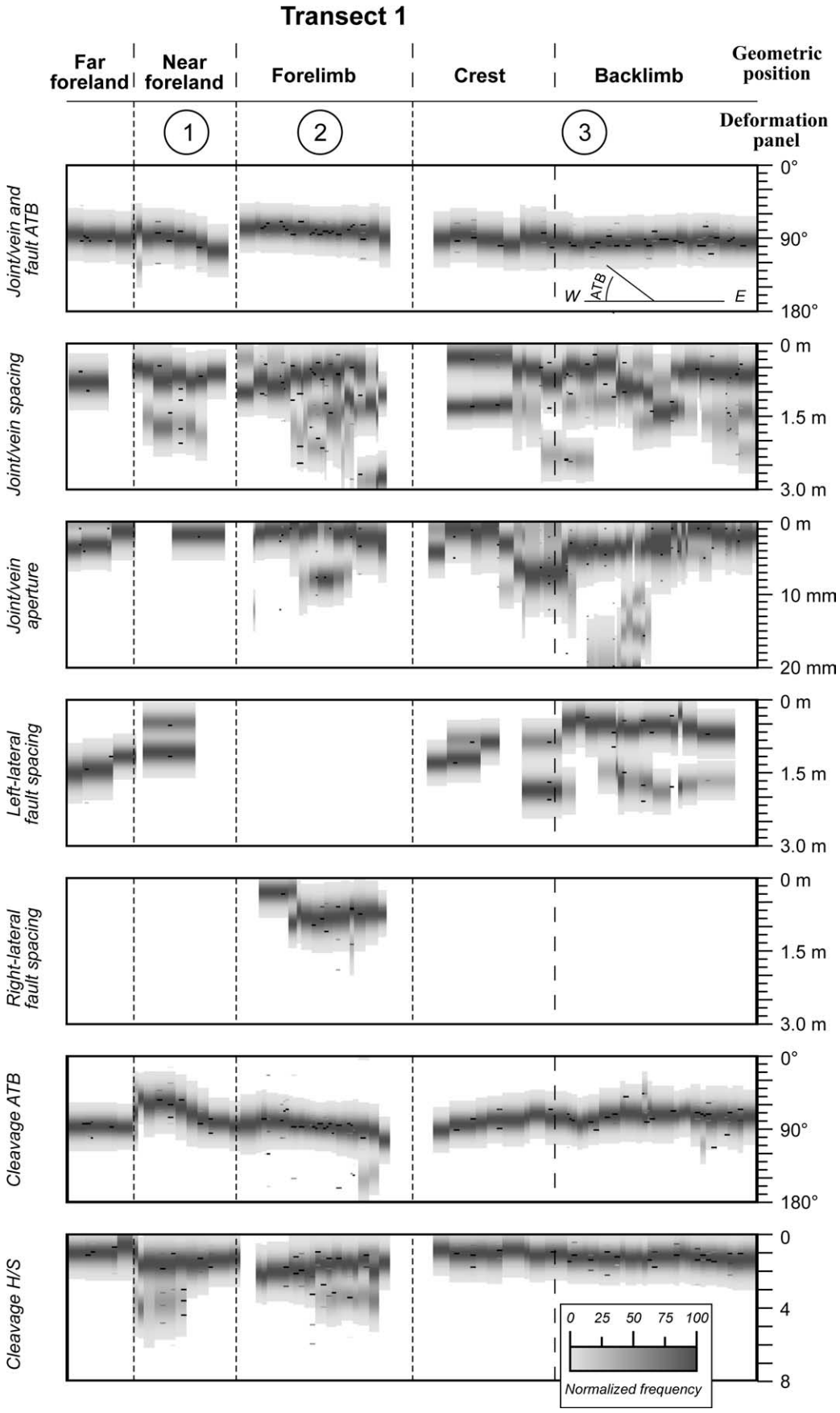

Fig. 10. Structural data projected onto transect Tr1. Dark dashes represent data values, grey area represents the smoothed Gaussian fit and normalised frequency is represented in grey-tones scale. See text for details and Fig. 6 for location.

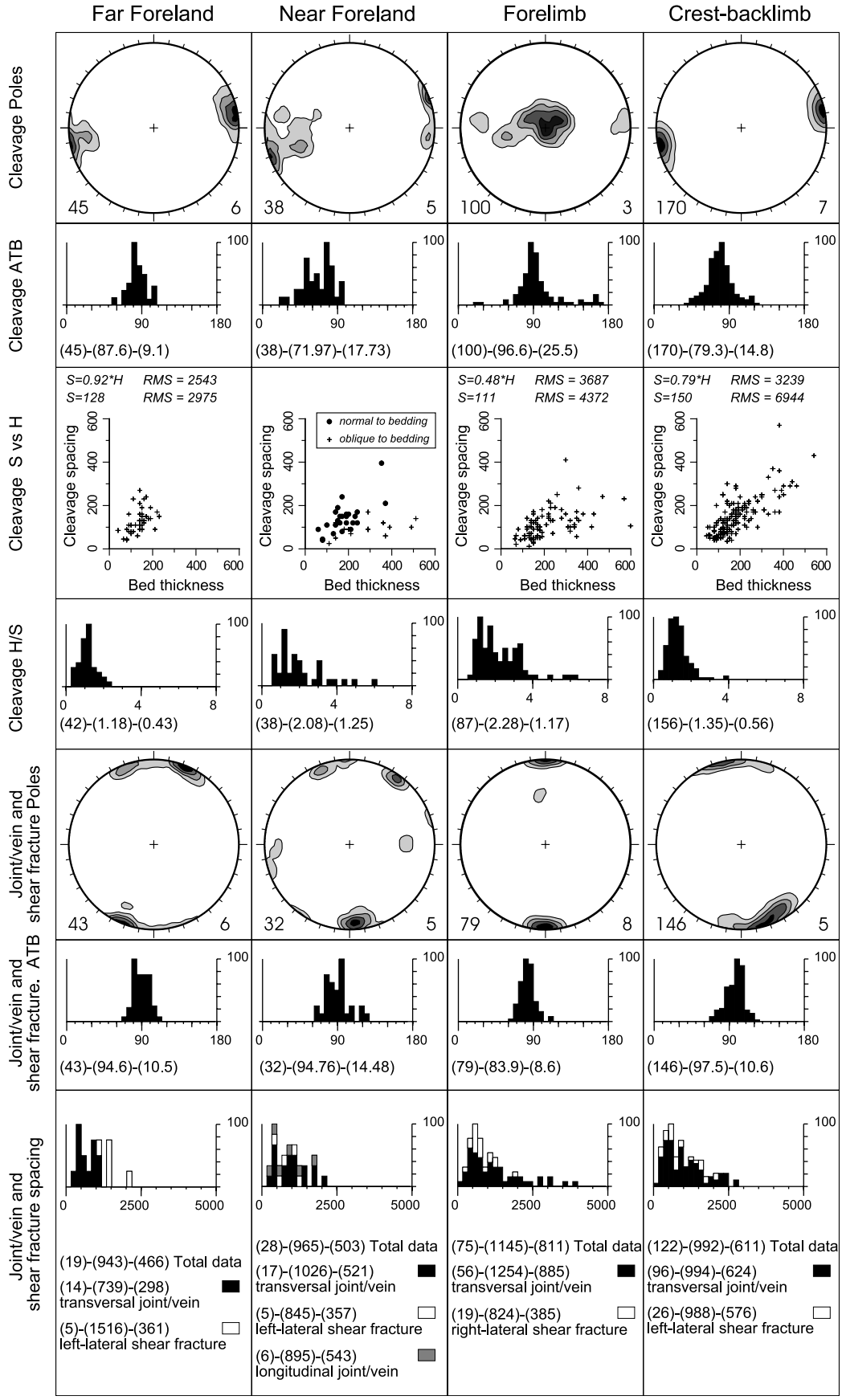

Fig. 11. Characterisation of deformation panels by frequency histograms of angle to bedding (ATB), *H*/*S*, and spacing, *H*–*S* scatterograms, unfolded cumulative contoured stereonets of poles to solution cleavage, and joints, veins and faults. Numbers in the left-bottom and right-bottom corners of the stereonets are number of data and percentage of contouring interval, respectively. Numbers below the frequency histograms indicate, from the left to the right, the number of data, the average value and the standard deviation.

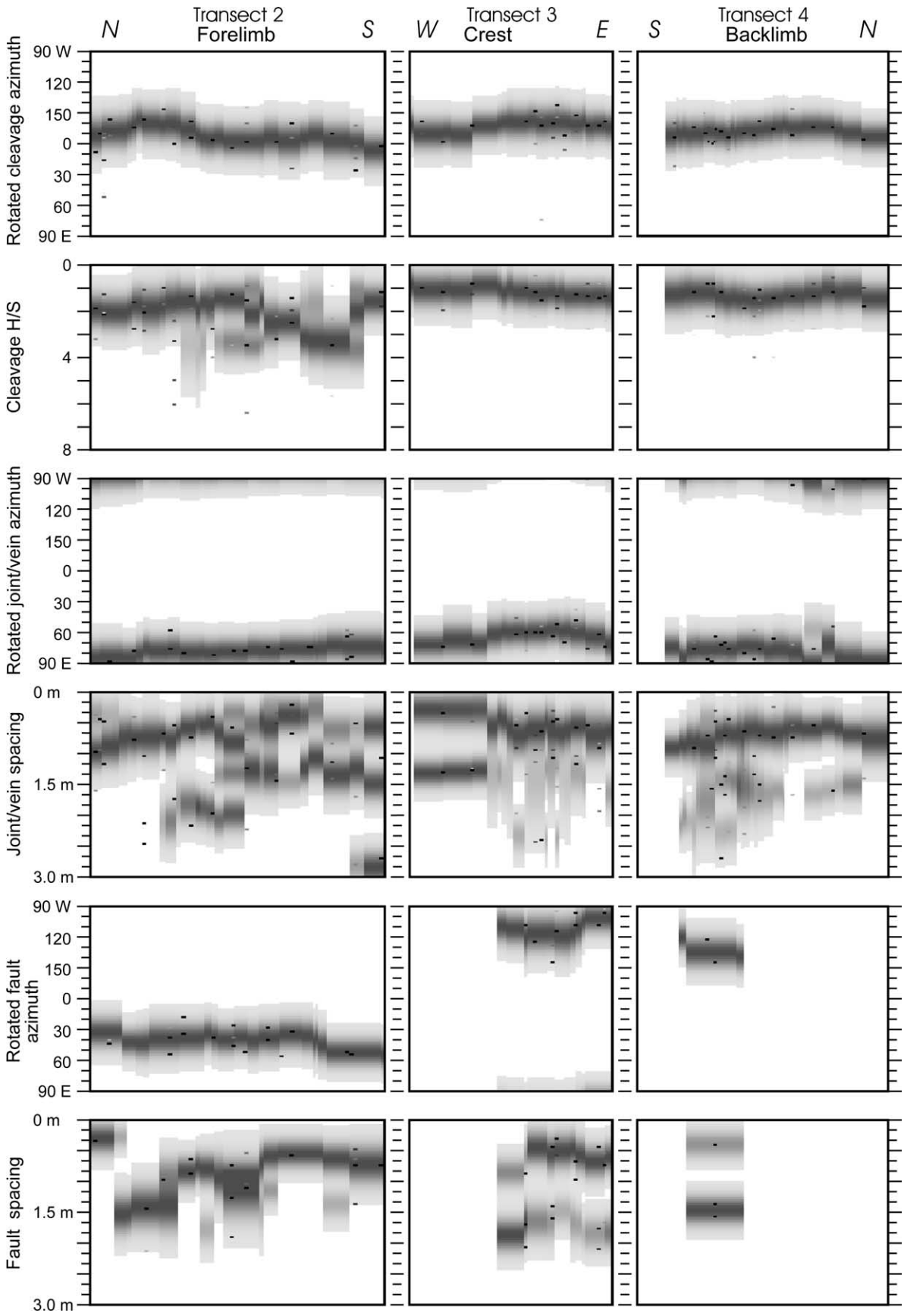

Fig. 12. Structural transects 2 (along the forelimb, left), 3 (across the crest, centre) and 4 (along the backlimb, right). Transect locations are shown in Fig. 6. Data presentation as in Fig. 9.

The importance of the second and third cleavage sets lies in the information they provide for constraining anticlinal kinematics. Joints and veins are nearly vertical with a strike of 87° (±14°) and are nearly bed-orthogonal (ATB = 84 ± 10°). Right-lateral faults strike 83° (±18°) and are southward dipping (61 ± 11°), but nearly bed-orthogonal (92 ± 13°). The rotated azimuthal analysis of both joints/veins and faults shows rather constant azimuthal values along the forelimb (Fig. 12). Average fracture spacing is 1145 mm (±811 mm), 1254 mm (±885 mm) and 824 mm (±385 mm) for joints/veins and faults, respectively.

In the crest/backlimb deformation panel, solution cleavage strikes nearly parallel to the fold axis (169 ± 12°) and is nearly perpendicular to bedding (80 ± 15°) (Fig. 11). The cleavage *H*, *S* dataset has a regression line with a slope of 0.79 (RMS is 3239); the horizontal regression line has a *Y*-intercept of 150 (RMS is 6944). The cleavage *H*/*S* ratio is unimodal with an average value of 1.4 (±0.6) (Fig. 11). Joints/veins in the crest/backlimb deformation panel strike nearly perpendicular to the fold axis (76 ± 25°) and are perpendicular to bedding (ATB = 98 ± 11°). Rare left-lateral faults occur in the eastern part of the periclinal closure and in the southern part of the backlimb (Fig. 12). The cumulative average spacing of joints/veins and faults is 992 mm (±611 mm). When only tensile structures are considered, the average spacing is 994 mm (±624 mm). The average spacing of faults is 988 mm (±576 mm).

Finally, data in the far foreland are described for comparison. In this area, nearly vertical solution cleavages strike parallel (168 ± 11°) to the Añisclo anticline axial trend (171°) and are roughly perpendicular to bedding (ATB = 88 ± 9°) (Fig. 11). Cleavage spacing increases with increases of the corresponding bed thickness. If a linear through the origin fit is adopted, the regression line slope is 0.92, with the residual mean square (RMS) being 2543. On the other hand, if a regression line with 0 slope is assumed, the *Y*-intercept is 128 mm and the corresponding RMS is 2975. *H*/*S* data are unimodal with an average value of 1.2 (±0.4). Joints and veins strike orthogonal to cleavage (azimuth 69 ± 16°, dip 85 ± 11°), whereas left-lateral faults are oblique (azimuth 111 ± 16°, dip 85 ± 11°). Their spacing averages 739 mm (±298 mm) for joints/veins and 1516 mm (±361 mm) for faults.

4.2. Structural summary

The 3-D distribution of mesoscale structures in the Añisclo anticline and their overprinting relationships are schematically illustrated in Fig. 13. Longitudinal solution cleavages nearly perpendicular to bedding are distributed all around the anticline, as well as transverse joints/veins perpendicular to bedding. Mutual overprinting relationships indicate that these elements are coeval. The frequency (*H*/*S*) of this longitudinal cleavage set is unimodal in the crest–backlimb deformation panels and in the far foreland. *H*/*S* values and their standard deviations increase in the forelimb panel and in the near foreland. The longitudinal cleavage set near perpendicular to bedding is overprinted in the forelimb and in the near foreland by an oblique to bedding, longitudinal solution cleavage set. After correcting for bedding dip, this set has a forelandward dip in the forelimb, indicating top-to-the-crest layer-parallel shear and a hinterlandward dip in the near foreland, indicating top-to-the-foreland layer-parallel shear. In the forelimb, both bedding-orthogonal and oblique to bedding cleavages are overprinted by a nearly vertical solution cleavage set that is sub-parallel to bedding (Fig. 13). Dextral faults occur along the forelimb and are coeval to both the bedding-orthogonal longitudinal cleavage and to transverse joints/veins. Accordingly, dextral faults are characteristic of the forelimb deformation panel (Fig. 13). Sinistral faults occur locally in the crest and in the backlimb sectors.

5. Discussion

5.1. cleavage spacing versus bed thickness

The *H*/*S* ratio has been used in our work to allow direct comparison of deformation intensities in beds of different thickness. This ratio is widely used for joints and veins (e.g. Price, 1966; Hobbs, 1967; McQuillan, 1973; Narr and Suppe, 1991; Gross, 1993), where the spacing to thickness ratio can be assumed to be linear for bed thickness less than 1 m (e.g. Ladeira and Price, 1981; Huang and Angelier, 1989; Gross et al., 1995). Similarly, our dataset indicates that the cleavage spacing depends on the bed thickness. In particular, the RMS values associated with the linear through the origin fit (hypothesis that *S* relates to *H*) is systematically lower than the RMS associated with the linear fit where the slope is imposed to be 0 (hypothesis that *S* does not relate to *H*), with the exception of the cleavage oblique to bedding in the near foreland. This set is characterised by higher *H*/*S* values, thus suggesting that *S* linearly relates to *H* until a given deformation intensity. Above this threshold value, *S* becomes independent of *H*. A relationship between cleavage spacing and bed thickness was also found by other authors (e.g. Durney and Kisch, 1994; Casas et al., 1996; Sans et al., 2003), thus supporting the validity of the *H*/*S* ratio for comparing deformation intensity in different fold sectors, instead of *S*, as commonly used in the past (e.g. Alvarez et al., 1978).

5.2. Pre- versus syn-folding layer parallel shortening

The main solution cleavage set in the Añisclo anticline is nearly perpendicular to bedding all along the fold, which is a necessary geometric condition to support a pre-folding origin (e.g. Protzman and Mitra, 1990; Averbuch et al., 1992; Harris and Van Der Pluijm, 1998). Previous studies have shown that the development of cleavage perpendicular to bedding in limestone commonly initiates before map-scale folding (e.g. Allmendinger, 1982; Mitra et al., 1984; Casas and Muñoz, 1987; Clendenen et al., 1988; Averbuch et al., 1992; Tavernelli, 1997; Sans et al., 2003, among others). The cross-sectional variability of cleavage *H*/*S* in the Añisclo anticline, however, cannot be explained by a pre-folding origin of cleavage. Indeed, it provides support to a syn-folding origin of this cleavage set. These apparently contrasting features can be reconciled by associating the

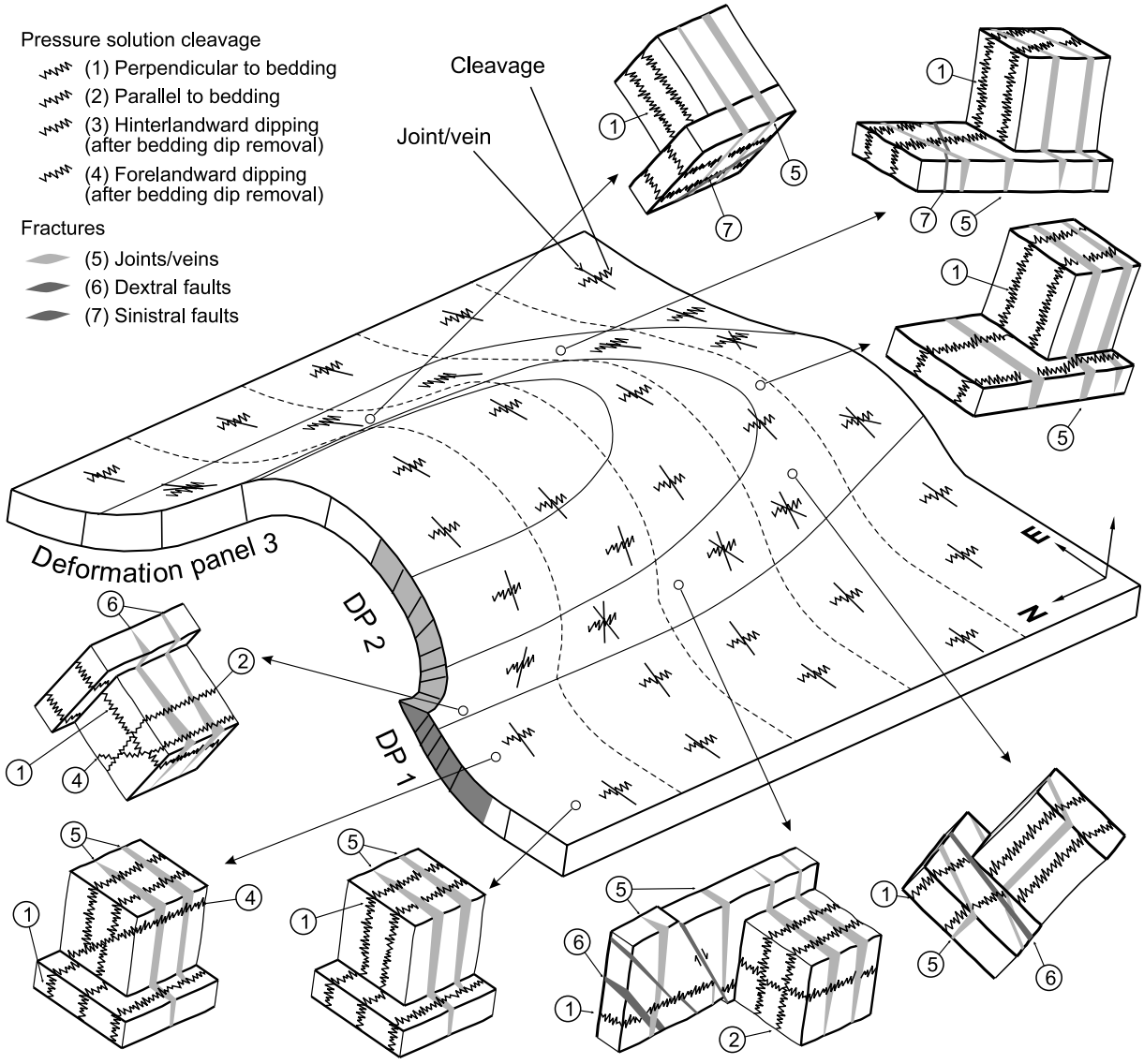

Fig. 13. Schematic illustration of the spatial distribution of mesoscale structures and their crosscutting relationships. See text for details.

occurrence of layer-parallel shortening and cleavage development with the initial forelandward propagation of the basal thrust (e.g. Marshak and Engelder, 1985; Geiser, 1988; Evans and Dunne, 1991) and early stage of fold nucleation and amplification, when hinge zones do not yet favour deformation localisation in the different fold sectors (e.g. Storti et al., 1997). The well-layered nature of the deforming rocks ensures flexural slip folding and development of bed-orthogonal cleavage within competent layers (e.g. Helmstaedt and Greggs, 1980). Development of solution cleavages nearly perpendicular to bedding during early folding indicates that flexural slip was very efficient and produced a negligible component of layer parallel shear (e.g. Tavani et al., 2004). According to this interpretation, the development of layer-parallel shortening preceding significant fold amplification is an integral part of the folding process. Solution cleavages associated with this layer-parallel shortening event have to be regarded as kinematically syn-folding structures, despite the geometric criterion that would suggest a pre-folding origin.

5.3. Line-length variation during folding

Finite strain data in the northern part of the Añisclo anticline (Holl and Anastasio, 1995) allow us to attempt a quantitative estimation of layer-parallel shortening values from cleavage frequency. The strain ellipsoids are oblate with minimum axes (Z) perpendicular to cleavage (Holl and Anastasio, 1995), which supports a geometric relationship between strain accumulation and cleavage development. Accordingly, we assumed that layer-parallel shortening occurred at constant thickness by development of longitudinal bed-normal cleavage. Finite strain data by Holl and Anastasio (1995) indicate 21% shortening in the backlimb of the northern Añisclo anticline, 22% in the crest and 21.3 and 25% in the forelimb. We correlated the average H/S value of the longitudinal bed-normal solution cleavage set in the crest–backlimb deformation panel ($H/S = 1.4$) with the average finite strain value for these domains in the northern part of the anticline (21.5%),

particularly as these domains have comparable geometry all along the length of the Añisclo anticline. This correlation provided the background magnitude of shortening prior to deformation localisation in the forelimb and the near foreland. An estimate of localised shortening in the forelimb and the near foreland was obtained by assuming a linear relationship between *H*/*S* values of the solution cleavage and finite strain. With this assumption, the average *H*/*S* value of 2.28 in the forelimb corresponds to shortening of 36.3%. By subtracting the background deformation to the total amount, we obtained a partitioning of shortening into 21.5% prior to deformation localisation and 14.8% due to deformation localisation. Applying the same reasoning to the near foreland provides an estimate of 33.1% as the cumulative shortening with 11.6% after deformation localisation. The regional-scale of the Holl and Anastasio (1995) work does not ensure the lithologic match between strain and *H*/*S* data and this certainly affected our computations. Despite this, the magnitude of the estimated amount of shortening shows that syn-folding line-length variations have to be considered during cross-section restorations (e.g. Protzman and Mitra, 1990; McNaught and Mitra, 1996; Smart et al., 1999; Hogan and Dunne, 2001).

5.4. Fold evolution

Comparison between fold geometry in Figs. 4 and 5 supports the evolution of the Añisclo anticline by décollement folding followed by thrust breakthrough and fault-propagation folding, under the assumption that the lateral variability of fold geometry and kinematics is representative of the time progression of fault–fold interaction (e.g. Mueller and Suppe, 1997; Poblet et al., 1998; Apotria and Wilkerson, 2002). Such an inferred evolutionary pathway is supported by the deformation pattern of the Añisclo anticline. Unification of the backlimb and crest into deformation panel 3 and the comparison with deformation pattern in the far foreland indicate that their characteristic solution cleavage pattern represents a background deformation produced in an early stage dominated by a forelandward migration of the basal thrust tip and embryonic folding (Fig. 14a and b) (e.g. Geiser, 1988). The amount of layer-parallel shortening during this stage can be assumed constant through the multilayer because cleavage is about orthogonal to bedding and corresponds to about 21% as a maximum. During this initial folding stage, the shape was nearly symmetric with shallow dipping limbs and with a large wavelength to amplitude ratio (*w*/*a* is about 10), as commonly recognised for embryonic décollement anticlines (e.g. De Sitter, 1956; Mitra, 2003, and references therein). The folding process was ensured by flow of ductile material from the leading and trailing synclines into the anticlinal core (e.g. Wiltschko and Chapple, 1977; Poblet et al., 1998; Mitra, 2003), until the thickness of the Keuper evaporites become lower than the minimum required for efficient flow. Such an out-of-the-syncline flow of the Triassic evaporites is supported by the evidence that they are missing in adjacent synclinal structures (e.g. Poblet et al., 1998; Fernandez, 2004). Welding of synclinal areas to the basal décollement inhibited décollement

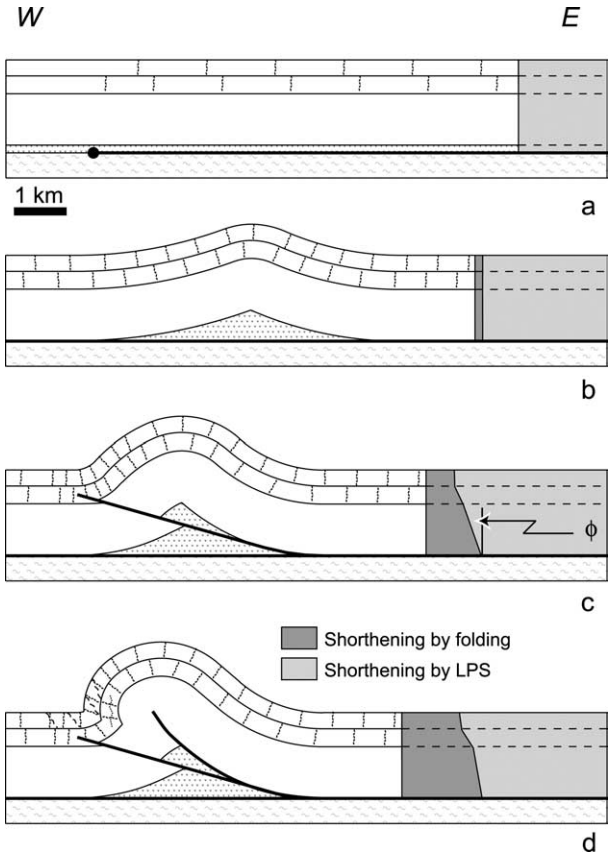

Fig. 14. Proposed kinematic evolution of the Añisclo anticline with progressive development of longitudinal solution cleavage sets and partitioning of shortening into LPS and folding. See text for details.

folding and favoured deformation localization and further fold amplification by fault-propagation folding (Fig. 14c). Infilling of the main solution cleavage set in the forelimb and near foreland of the anticline occurred during this fault-propagation stage (Suppe and Medwedeff, 1990), when deformation panels 1 and 2 formed. The occurrence of line-length variations at constant thickness supports deformation by double-edge fault-propagation folding (e.g. Tavani et al., 2006), where the cumulative shortening along the basal décollement is partitioned into folding and layer-parallel shortening in the layers stratigraphically overlying the ramp tip (Fig. 15a). In this model, the amount of layer-parallel shortening can be defined by the angle ϕ (Fig. 15a). In the simplest configuration, i.e. when the regional dip (ρ) is 0° and the footwall cutoff angle equals the ramp step-up angle (θ). The angle ϕ relates to both θ and β (hanging wall cutoff angle) through equation (6) in Tavani et al. (2006):

$$\tan(\phi) = \cot(\theta) - \cot(\beta) + (\theta - \beta) \quad (1)$$

When the regional dip is $\neq 0$ and the initial footwall cutoff angle (θ^*) differs from θ, Eq. (1) can be written as:

$$\tan(\phi) = \cot(\theta^*) - \cot(\beta) + (\theta^* - \beta) \quad (2)$$

θ^* and β can also be expressed as:

$$\theta^* = \eta f + \theta + \rho \quad (3)$$

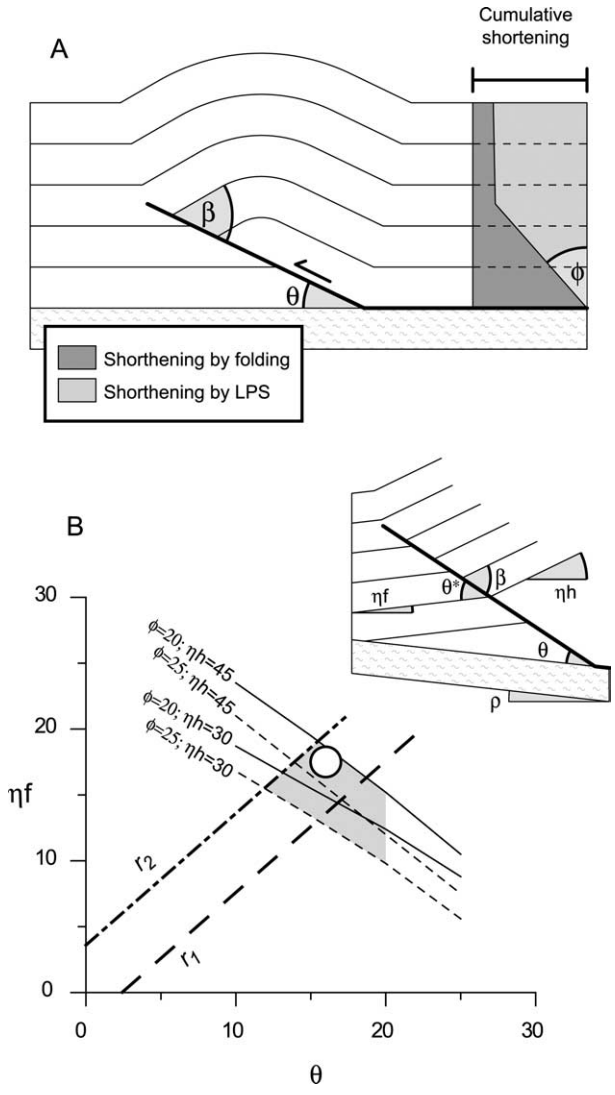

Fig. 15. (a) Geometry of a double-edge fault-propagation anticline developed above a ramp nucleated from the basal décollement and propagated upward at a constant rate. (b) Graphical solutions for Eq. (5). The grey area indicates the variability field of the step-up angle of the ramp and footwall dip (ηh) during the main fault-propagation folding stage of the Añisclo anticline. The white circle indicates our best value obtained by try and error balancing of the cross-section in Fig. 5.

$$\beta = \eta h + \theta + \rho \tag{4}$$

with ηf and ηh being the footwall and hanging wall dip, respectively (Fig. 15b). By substituting Eqs. (3) and (4) into Eq. (2) we obtain:

$$\tan(\phi) = \cot\left(\eta f + \theta + \rho\right) - \cot\left(\eta h + \theta + \rho\right) + (\eta f - \eta h) \tag{5}$$

The regional dip in the Añisclo anticline is 2.4° and the estimated ϕ is 22°. The forelimb dip in the areas not affected by late stage anticlinal breakthrough ranges between 30 and 45°. This implies that in the Añisclo anticline, Eq. (5) can be verified by different values of ηf and θ. The graph in Fig. 15b shows the relationships between ηf and θ for different values of ϕ and ηf. Additional constraints for the fault–fold pair reconstruction can be obtained by considering that: (i) θ cannot exceed 20°, otherwise the ramp would emerge; (2) in our reconstruction, the ramp cuts across the Keuper and θ does not exceed the dip of backlimb. In the case of a symmetric décollement anticline (forelimb dip = backlimb dip + 2ρ), the solution in the graph of Fig. 15b must lie below the line r_1. In the case of a slightly asymmetric décollement anticline (forelimb dip = backlimb dip + 2ρ + 10°), the solution must lie below the r_2 line. The grey area in Fig. 15b represents the range of possible solutions and the white circle represents the proposed solution for the Añisclo anticline ($\theta = 16°$; $\eta f = 17°$), which was obtained by trial and error during cross-section balancing. Cumulative displacement at the end of this fault-propagation folding stage was about 30% of the original cross-sectional length (Fig. 14c). Active hinge folding (e.g. Suppe et al., 1992) characterised this stage of anticlinal growth as indicated by the lack of field evidence supporting a significant amount of bed-parallel shear (i.e. large deviations of cleavage ATB from 90°) in the forelimb and in the near foreland, which is required by fixed-hinge folding (e.g. Erslev and Mayborn, 1997).

The progression of folding and the progressive steepening of the forelimb eventually caused fold tightening and locking (e.g. Ramsay, 1974; Allmendinger, 1982). This triggered anticlinal breakthrough fault-propagation folding (Suppe and Medwedeff, 1990) along a steeper ramp emanating from the backlimb and localised at the top of the evaporites (Fig. 14d). During this late-stage folding event, new solution cleavage surfaces oblique to bedding overprinted the main solution cleavage set in the forelimb and in the near foreland of the anticline. The symmetric distribution of shear senses away from the leading synclinal hinge supports fixed-hinge flexural-slip folding, where material was not able to migrate across axial surfaces (e.g. Suppe et al., 1992). Furthermore, solution cleavages parallel to bedding developed in the steeply dipping to upright and overturned forelimb. Hanging wall translation above the high angle fault during the late stage anticlinal breakthrough caused an additional folding-related shortening of about 4% and a slight line-length modification, with an across-strike extension of less than 2% in the upper multilayer sectors.

6. Conclusions

Quantitative analysis of the folding-related deformation pattern in the Añisclo anticline of the Southern Pyrenees can be summarised as follows:

(1) Folding was accompanied by the development of longitudinal pressure-solution cleavages and transverse joints and veins that bisect less abundant dextral and sinistral shear fracture arrays.
(2) The spacing of the main pressure-solution cleavage set relates to the corresponding bed thickness. This sensitivity to layer thickness is analogous to what is widely described for tensile structures, despite their different origins. Given the importance of pressure solution in the deformation of the upper crust, such an analogy deserves to be further

investigated by specific work.

(3) Pressure-solution cleavage exhibits a spatial distribution, which is related to the position within the anticline. The same behaviour does not characterise joints and veins. Solution cleavages are the most appropriate structures for making inferences on fold kinematics, using both their normalised frequency (*H*/*S* ratio) and angle to bedding (ATB). The spatial distribution of these two parameters individuates three major deformation panels labelled near foreland, forelimb and crest–backlimb. Development of these deformation panels started in a delocalised way by a background deformation, later overprinted by a selective infilling of solution cleavage in the near foreland and in the forelimb during the localised deformation stage.

(4) Correlation between the normalised frequency of solution cleavage and finite strain data available in the literature indicates approximately 21.5% of line-length reduction by layer-parallel shortening during the delocalised stage (early stages of folding), followed by 14.8 and 11.6% of further line-length reduction in the forelimb and near foreland sectors, respectively. This result provides a cautionary note to the common assumption of line-length preservation in cross-section balancing of fault-related folds deforming carbonate multilayers.

(5) Sequential restoration of the deformation pattern in the Añisclo anticline indicates that fold evolution started by forelandward propagation of the basal décollement in the Keuper evaporites together with layer-parallel shortening and incipient folding. With increasing contraction, the anticline initially grew by décollement folding, followed by both low- and high-angle breakthrough fault-propagation folding.

(6) The working method specifically designed for the 3-D analysis of deformation patterns in faulted and folded terrains provides an effective tool for unravelling fault–fold kinematics.

Acknowledgements

We gratefully acknowledge constructive reviews and advice from D.J. Anastasio and B. Dunne. In particular, the very detailed review from B. Dunne allowed us to significantly improve the manuscript. The statistical analysis of structural data was performed by the Daisy 3 software, available for free download at http://host.uniroma3.it/progetti/fralab/. Funding to F. Salvini, F. Storti and S. Tavani was provided by the Italian MIUR (Ministero dell'Istruzione, dell'Università e della Ricerca), grants awarded to F. Salvini. O. Fernandez and J.A. Muñoz wish to acknowledge support from the Generalitat de Catalunya (Grup de Recerca de Geodinàmica i Anàlisi de Conques, 2001SGR-000074) and from the MCyT (Proyectos CGL2004-05816-C02-01). Research by O. Fernández was made possible by a pre-doctoral grant from the Direcció General de Recerca (Generalitat de Catalunya).

References

Allmendinger, R.W., 1982. Analysis of microstructures in the Meade plate of the Idaho–Wyoming foreland thrust belt, U.S.A.. Tectonophysics 85, 221–251.

Alvarez, W., Engelder, T., Geiser, P.A., 1978. Classification of solution cleavage in pelagic limestones. Geology 6, 263–266.

Anastasio, D.J., Fisher, D.M., Messina, T.A., Holl, J.E., 1997. Kinematics of décollement folding in the Lost River Range Idaho. Journal of Structural Geology 19, 355–368.

Apotria, T.G., Wilkerson, M.S., 2002. Seismic expression and kinematics of a fault-related fold termination: Rosario structure, Maracaibo Basin, Venezuela. Journal of Structural Geology 24, 671–687.

Apotria, T.G., Wilkerson, M.S., Knewtson, S.L., 1996. 3D geometry and controls on fracturing in a natural fault-bend fold: Rosario Field, Maracaibo Basin, Venezuela. American Association of Petroleum Geologists Bulletin 80, 1268.

Averbuch, O., Frizon de Lamotte, D., Kissel, C., 1992. Magnetic fabric as a structural indicator of the deformation path within a fold-thrust structure: a test case from the Corbières (NE Pyrenees, France). Journal of Structural Geology 14, 461–474.

Casas, J.M., Muñoz, J.A., 1987. Sequences of mesostructures related to the development of Alpine thrusts in the Eastern Pyrenees. Tectonophysics 135, 67–75.

Casas, J.M., Durney, D., Ferret, J., Munoz, J.A., 1996. Determinacion de la deformacion finita en la vertiente sur del Pirineo oriental a lo largo de la transversal del rio Ter. Geogaceta 20, 803–805.

Chester, J.S., 2003. Mechanical stratigraphy and fault-fold interaction, Absaroka thrust sheet, Salt River Range, Wyoming. Journal of Structural Geology 25, 1171–1192.

Chester, J.S., Logan, J.M., Spang, J.H., 1991. Influence of layering and boundary conditions on fault-bend and fault-propagation folding. American Association of Petroleum Geologists Bulletin 103, 1059–1072.

Clendenen, W.S., Kligfield, R., Hirt, A.M., Lowrie, W., 1988. Strain studies of cleavage development in the Chelmsford Formation, Sudbury Basin, Ontario. Tectonophysics 145, 191–211.

Cooper, M., 1992. The analysis of fracture systems in subsurface thrust structures from the foothills of the Canadian Rockies. In: McClay, K.R. (Ed.), Thrust Tectonics. Chapman and Hall, London, pp. 391–405.

Corbett, K., Friedmean, M., Spang, J., 1987. Fracture development and mechanical stratigraphy of Austin Chalk, Texas. American Association of Petroleum Geologists Bulletin 71, 17–28.

Couzens, B.A., Dunne, W.M., 1994. Displacement transfer at thrust terminations: the Saltville thrust and Sinking Creek anticline, Virginia, U.S.A.. Journal of Structural Geology 16, 781–793.

Couzens, B.A., Wiltschko, D.V., 1996. The control of mechanical stratigraphy on the formation of triangle zones. Bulletin of Canadian Petroleum Geologists 44, 165–179.

Dahlstrom, C.D.A., 1990. Geometric constraints derived from the law of conservation of volume and applied to evolutionary models for detachment folding. American Association of Petroleum Geologists Bulletin 74, 336–344.

De Sitter, L.V., 1956. Structural Geology. McGraw-Hill, New York.

Dinarès Turell, J., 1992. Paleomagnetisme a les unitats sudpirinenques superiors. Implicacions estructurals. PhD thesis, University of Barcelona.

Durney, D.W., Kisch, H.J., 1994. A field classification and intensity scale for first-generation cleavages. Journal of Australian Geology & Geophysics 15, 257–295.

Erslev, E.A., Mayborn, K.R., 1997. Multiple geometries and modes of fault-propagation folding in the Canadian thrust belt. Journal of Structural Geology 19, 321–335.

Evans, M.A., Dunne, W.M., 1991. Strain factorization and partitioning in the North Mauntain thrust sheet, central Appalachians, U.S.A. Journal of Structural Geology 13, 21–35.

Fernandez, O., 2004. Reconstruction of geological structures in 3D. An example from the southern Pyrenees. PhD thesis, University of Barcelona.

Fernández, O., Muñoz, J.A., Arbués, P., Falivene, O., Marzo, M., 2004. Three-dimensional reconstruction of geological surfaces: an example of growth strata and turbidite systems from the Ainsa basin (Pyrenees, Spain). American Association of Petroleum Geologists Bulletin 88, 1049–1068.

Fischer, M.P., Jackson, P.B., 1999. Stratigraphic controls on deformation patterns in fault-related folds: a detachment fold example from the Sierra Madre Oriental, northeast Mexico. Journal of Structural Geology 21, 613–633.

Fischer, M.P., Woodward, N.B., Mitchell, M.M., 1992. The kinematics of break-thrust folds. Journal of Structural Geology 14, 451–460.

Fisher, D.M., Anastasio, D.J., 1994. Kinematic analysis of a large-scale leading edge fold, Lost River Range, Idaho. Journal of Structural Geology 16, 337–354.

Fisher, M.W., Coward, M.P., 1982. Strain and folds within thrusts sheets: an analysis of the Heilam sheet, northwest Scotland. Tectonophysics 88, 291–312.

Garrido, A., Rios, L.M., 1972. Síntesis geológica del Secundario y Terciario entre los ríos Cinca y Segre (Pirineo central de la vertiente surpirenaica, provincias de Huesca y Lérida). Boletín del Instituto Geológico y Minero de España 83, 1–47.

Geiser, P.A., 1988. Mechanisms of thrust propagation: some examples and implications for the analysis of overthrust terranes. Journal of Structural Geology 10, 829–845.

Gross, M.R., 1993. The origin and spacing of cross joints: examples from the Monterey Formation, Santa Barbara coastline, California. Journal of Structural Geology 15, 737–751.

Gross, M.R., 1995. Fracture partitioning: failure mode as a function of lithology in the Monterey Formation of coastal California. Geological Society of America Bulletin 107, 779–792.

Gross, M.R., Fischer, M.P., Engelder, T., Greenfield, R.J., 1995. Factors controlling joint spacing in interbedded sedimentary rocks: integrating numerical models with field observations from the Monterey Formation, U.S.A.. In: Ameen, M.S. (Ed.), Fractography: Fracture Topography as a Tool in Fracture Mechanics and Stress Analysis Geological Society Special Publication 92, pp. 215–233.

Hancock, P.L., 1985. Brittle microtectonics: principles and practice. Journal of Structural Geology 7, 437–457.

Harris, J.H., Van Der Pluijm, B.A., 1998. Relative timing of calcite twinning strain and fold–thrust belt development; Hudson Valley fold–thrust belt, New York, U.S.A.. Journal of Structural Geology 20, 21–31.

Hedlund, C.A., Anastasio, D.J., Fisher, D.M., 1994. Kinematics of fault-related folding in a duplex, Lost River Range, Idaho, U.S.A.. Journal of Structural Geology 16, 571–584.

Helmstaedt, H., Greggs, R.G., 1980. Stylolitic cleavage and cleavage refraction in Lower Paleozoic carbonate rocks of the Great Valley, Maryland. Tectonophysics 66, 99–114.

Hobbs, D.W., 1967. The formation of tension joints in sedimentary rocks: an explanation. Geological Magazine 104, 550–556.

Hogan, J.P., Dunne, W.M., 2001. Calculation of shortening due to outcrop-scale deformation and its relation to regional deformation patterns. Journal of Structural Geology 23, 1507–1529.

Holl, J.E., Anastasio, D.J., 1995. Cleavage development within a foreland fold and thrust belt, southern Pyrenees, Spain. Journal of Structural Geology 17, 357–369.

Huang, Q., Angelier, J., 1989. Fracture spacing and its relation to bed thickness. Geological Magazine 126, 355–362.

Jamison, W.R., 1992. Stress controls of fold thrust style. In: McClay, K.R. (Ed.), Thrust Tectonics. Chapman and Hall, London, pp. 155–164.

Jamison, W.R., 1997. Quantitative evaluation of fractures on Monkshood Anticline, a detachment fold in the foothills of western Canada. American Association of Petroleum Geologists Bulletin 81, 1110–1132.

Ladeira, F.L., Price, N.J., 1981. Relationship between fracture spacing and bed thickness. Journal of Structural Geology 3, 179–183.

Lemiszki, P.J., Landes, J.D., Hatcher Jr., R.D., 1994. Controls on hinge-parallel extension fracturing in single-layer tangential-longitudinal strain folds. Journal of Geophysical Research 99, 22,027–22,042.

Marshak, S., Engelder, T., 1985. Development of cleavage in limestones of a fold–thrust belt in eastern New York. Journal of Structural Geology 7, 345–359.

McNaught, M.A., Mitra, G., 1996. The use of finite strain data in constructing a retrodeformable cross-section of the Meade thrust. Journal of Structural Geology 185, 573–583.

McQuillan, H., 1973. Small-scale fracture density in Asmari Formation of southwest Iran and its relation to bed thickness and structural setting. American Association of Petroleum Geologists Bulletin 57, 2367–2385.

Millán, H., 1996. Estructura del frente de cabalgamiento surpirenaico en las Sierras Exteriores Aragonesas. PhD thesis, Univ. de Zaragoza.

Mitchell, M.M., Woodward, N.B., 1988. Kink detachment fold in the southwest Montana fold and thrust belt. Geology 16, 162–165.

Mitra, G., Yonkee, W.A., Gentry, D.J., 1984. Solution cleavages and its relationship to major structures in the Idaho–Utah–Wyoming thrust belt. Geology 12, 354–358.

Mitra, S., 2003. A unified kinematic model for the evolution of detachment folds. Journal of Structural Geology 25, 1659–1673.

Mueller, K., Suppe, J., 1997. Growth of Wheeler Ridge anticline, California: geomorphic evidence for fault-bend folding behaviour during earthquakes. Journal of Structural Geology 19, 383–396.

Mukul, M., Mitra, G., 1998. Finite strain and strain variation analysis in the Sheeprock Thrust Sheet: an internal thrust sheet in the Provo salient of the Sevier Fold-and-Thrust belt, Central Utah. Journal of Structural Geology 20, 385–405.

Narr, W., Suppe, J., 1991. Joint spacing in sedimentary rocks. Journal of Structural Geology 13, 1037–1048.

Parés, J.M., Dinarès Turell, J., 1993. Magnetic fabric in two sedimentary rock-types from the Southern Pyrenees. Journal of Geomagnetism and Geoelectricity 45, 193–205.

Poblet, J., Muñoz, J.A., Trevé, A., Serra-Kiel, J., 1998. Quantifying the kinematic of detachment folds using the three-dimensional geometry: application to the Mediano anticline (Pyrenees Spain). Geological Society of America Bulletin 110, 111–125.

Price, N.J., 1966. Fault and Joint Development in Brittle and Semi-brittle Rocks. Pergamon Press, Oxford.

Protzman, G.M., Mitra, G., 1990. Strain fabric associated with the Meade thrust sheet: implications for cross-section balancing. Journal of Structural Geology 12, 403–417.

Pueyo, E.L., Pocoví, A., Millán, H., Sussman, A.J., 2004. Map-view models for correcting and calculating shortening estimates in rotated thrust fronts using paleomagnetic data. In: Sussman, A.J., Weil, A.B. (Eds.), Orogenic Curvature: Integrating Paleomagnetic and Structural Analyses Geological Society of America Special Publication 383, pp. 57–71.

Ramsay, J.G., 1967. Folding and Fracturing of Rocks. McGraw-Hill, New York. 568pp.

Ramsay, J.G., 1974. Development of chevron folds. Geological Society of America Bulletin 85, 1741–1754.

Rios, L.M., Lanaja, J.M., Frutos, E., 1982. Mapa geológico de España, Broto (30-9) sheet. IGME, scale 1:50,000.

Salvini, F., Storti, F., 2001. The distribution of deformation in parallel fault-related folds with migrating axial surfaces: comparison between fault-propagation and fault-bend folding. Journal of Structural Geology 23, 25–32.

Salvini, F., Storti, F., 2004. Active hinge folding-related deformation and its role in hydrocarbon exploration and development: insights from HCA modeling. In: McClay, K.R. (Ed.), Thrust Tectonics and Petroleum Systems American Association of Petroleum Geologists Memoirs 82, pp. 453–472.

Salvini, F., Billi, A., Wise, D.U., 1999. Strike-slip fault-propagation cleavage in carbonate rocks: the Mattinata Fault Zone, Southern Apennines, Italy. Journal of Structural Geology 21, 1731–1749.

Sanderson, D.J., 1982. Models of strain variation in nappes and thrust sheets: a review. Tectonophysics 88, 201–233.

Sans, M., Vergés, J., Gomis, E., Parés, J.M., Schiattarella, M., Travé, A., Calvet, F., Santanach, P., Doulcet, A., 2003. Layer parallel shortening in salt-detached folds: constraint on cross-section restoration. Tectonophysics 372, 85–104.

Seguret, M., 1970. Etude tectonique des nappes et series decollees de la partie centrale du versant sud des Pyrenees. PhD thesis, Univ. de Montpellier.

Smart, K.J., Krieg, R.D., Dunne, W.M., 1999. Deformation behavior during blind thrust translation as a function of fault strength. Journal of Structural Geology 21, 855–874.

Srivastava, D.C., Engelder, T., 1990. Crack-propagation sequence and pore-fluid conditions during fault-bend folding in the Appalachian Valley and Ridge, central Pennsylvania. Geological Society of America Bulletin 102, 116–128.

Stearns, D.W., 1968. Certain aspect of fracture in naturally deformed rocks. In: Rieker, R.E. (Ed.), National Science Foundation Advanced Science Seminar in Rock Mechanics. Special Report. Air Force Cambridge Research Laboratories, Bedford, Massachusetts, pp. 97–118. AD66993751.

Stewart, K.G., Alvarez, W., 1991. Mobile-hinge kinking in layered rocks and models. Journal of Structural Geology 13, 243–259.

Storti, F., Salvini, F., 1996. Progressive rollover fault-propagation folding: a possible kinematic mechanism to generate regional-scale recumbent folds in shallow foreland belts. American Association of Petroleum Geologist Bulletin 80, 174–193.

Storti, F., Salvini, F., 2001. Fault re-activation, fracture patterns, and cataclasite development in the carbonate rocks of the Narni Anticline. The evolution of a model trap structure in the Apennines, Italy. Journal of Petroleum Geology 24, 171–190.

Storti, F., Salvini, F., McClay, K., 1997. Fault-related folding in sandbox analogue models of thrust wedges. Journal of Structural Geology 19, 583–602.

Suppe, J., Medwedeff, D.A., 1990. Geometry and kinematics of fault-propagation folding. Ecoglae Geologicae Helvetiae 83, 409–454.

Suppe, J., Chou, G.T., Hook, S.C., 1992. Rates of folding and faulting determined from growth strata. In: McClay, K.R. (Ed.), Thrust Tectonics. Chapman and Hall, London, pp. 105–121.

Tavani, S., Louis, L., Souque, C., Robion, P., Salvini, F., Frizon de Lamotte, D., 2004. Folding related fracture pattern and physical properties of rocks in the Chaudrons ramp-related anticline (Corbières, France). In: Swennen, R., Roure, F., Granath, J. (Eds.), Deformation, Fluid Flow and Reservoir Appraisal in Foreland Fold and Thrust Belts. AAPG Hedberg Series 1. 257–275.

Tavani, S., Storti, F., Salvini, F., 2006. Double-edge fault-propagation folding: geometry and kinematics. Journal of Structural Geology 27, 19–35.

Tavernelli, E., 1997. Structural evolution of a foreland fold-and-thrust belt: the Umbria–Marche Apennines, Italy. Journal of Structural Geology 19, 523–534.

Teixell, A., 1996. The Ansó transect of the southern Pyrenees: basement and cover thrust geometries. Journal of the Geological Society 153, 301–310.

Thorbjornsen, K.L., Dunne, W.M., 1997. Origin of a thrust-related fold: geometrics vs. kinematic test. Journal of Structural Geology 19, 303–319.

Wiltschko, D.V., Chapple, W.M., 1977. Flow of weak rocks in Appalachian Plateau folds. American Association of Petroleum Geologists Bulletin 61, 653–670.

Woodward, N.B., 1999. Competitive macroscopic deformation processes. Journal of Structural Geology 21, 1209–1218.

Woodward, N.B., Rutherford Jr., E., 1989. Structural lithic units in external orogenic zones. Tectonophysics 158, 247–258.

Yonkee, A., 2005. Strain patterns within part of the Willard thrust sheet, Idaho–Utah–Wyoming thrust belt. Journal of Structural Geology 27, 1315–1343.